Title

Optimization of a depth of interaction encoding PET block detector for a PET/MRI insert

Permalink

https://escholarship.org/uc/item/1n167689

Journal

Physics in Medicine and Biology, 63(23)

ISSN

0031-9155

Authors

Selfridge, Aaron R
Cherry, Simon R
Judenhofer, Martin S

Publication Date

2018-12-01

DOI

10.1088/1361-6560/aaef59

Peer reviewed

Optimization of a depth of interaction encoding PET block detector for a PET/MRI insert

Aaron R Selfridge[1,3], **Simon R Cherry**[1,2], and **Martin S Judenhofer**[1,2]

[1]Department of Biomedical Engineering, UC Davis, Davis, California, United States of America

[2]Department of Radiology, UC Davis, Davis, California, United States of America

Abstract

Preclinical positron emission tomography, combined with magnetic resonance imaging (PET/MRI), is increasingly used as a tool to simultaneously characterize functional processes *in vivo.* Many emerging preclinical applications, however, are limited by PET detection sensitivity, especially when generating short imaging frames for quantitative studies. One such application is dynamic multifunctional imaging, which probes multiple aspects of a biological process, using relationships between the datasets to quantify interactions. These studies have limited accuracy due to the relatively low sensitivity of modern preclinical PET/MRI systems.

The goal of this project is to develop a preclinical PET/MRI insert with detection sensitivity above 15% (250–750 keV) to improve quantitation in dynamic PET imaging. To achieve this sensitivity, we have developed a detector module incorporating a 2 cm thick crystal block, which will be arranged into a system with 8 cm axial FOV, targeting mice and rats. To maintain homogenous spatial resolution, the detector will incorporate dual-ended depth-of-interaction (DOI) encoding with silicon photomultiplier (SiPM) based photodetector arrays. The specific aim of this work is to identify a detector configuration with adequate performance for the proposed system. We have optimized the SiPM array geometry and tested two crystal array materials with pitch ranging from 0.8 to 1.2 mm and various surface treatments and reflectors. From these configurations, we have identified the best balance between crystal separation, energy resolution, and DOI resolution.

The final detector module uses two rectangular SiPM arrays with 5×6 and 5×4 elements. The photodetector arrays are coupled to a 19×19 array of 1 mm pitch LYSO crystals with polished surfaces and a diffuse reflector. The prototype design has 14.3% ± 2.9% energy resolution, 3.57 ± 0.88 mm DOI resolution, and resolves all elements in the crystal array, giving it sufficient performance to serve as the basis for the proposed high sensitivity PET/MRI insert.

Keywords

positron emission tomography; magnetic resonance imaging; depth of interaction; silicon photomultiplier

[3]Author to whom any correspondence should be addressed. arselfridge@ucdavis.edu.

Introduction

High sensitivity small-animal PET imaging is receiving significant attention from commercial and academic entities inspired by new and demanding applications and changes in commercially available hardware (Ko *et al* 2016b, Hallen *et al* 2018, Vrigneaud *et al* 2018). Preclinical MRI, especially, is becoming a fundamental tool used to supplement PET data with additional morphological and functional information. Key use cases for combined PET/MRI include quantitative and dynamic studies that utilize synchronous acquisition of the two modalities, requiring improved detection sensitivity for PET imaging (Wehrl *et al* 2013, Ouyang *et al* 2014, Ouyang *et al* 2015). The wide availability of commercial MR compatible photodetectors, specifically SiPMs, has improved the feasibility of developing MR compatible PET systems, contributing to their increasing popularity and use (Roncali and Cherry 2011). These developments have strongly influenced preclinical PET as a field, and are clearly manifest in current commercial and academic systems (Disselhorst *et al* 2014, Mannheim *et al* 2018).

One promising application driving the development of simultaneous PET/MRI as a research tool is measurement of multiple functional aspects of a single transient process *in vivo* (Wehrl *et al* 2013, Ouyang *et al* 2015, Ko *et al* 2016b). Measurement of transient processes often requires that the target biology be imaged dynamically to extract meaningful information. In dynamic studies, increasing the PET detection sensitivity can allow either shorter imaging frames or improved image quality, and thus better quantitation. Subsequently, in dynamic studies best suited for simultaneous PET/MRI, high sensitivity is key for acquiring high quality data. High sensitivity has not been the foremost priority among available preclinical PET/MRI systems, with early systems serving mainly as a proof-of-concept. However, despite the proliferation of academic systems over the last 10 years sensitivity has not been a foremost priority (reported values are: 4.7% Vrigneaud *et al* (2018), 4.0% Hallen *et al* (2018), 3.4% Ko *et al* (2016a), 2.5% Sánchez *et al* (2012), 2.2% Stortz *et al* (2018), 1.2% Yamamoto *et al* (2012), 0.72% Omidvari *et al* (2017), 0.6% Mackewn *et al* (2015), 0.195% Yoon *et al* (2012)). The next generation of systems must overcome this sensitivity barrier without neglecting the established standard for high spatial resolution (Weissler *et al* 2015, Yang *et al* 2016). These developments in instrumentation will enable a range of applications requiring quantitative multifunctional measurement, where PET data must be temporally and spatially registered to MRI data.

We are currently developing a preclinical PET/MRI insert targeting simultaneous multifunctional imaging of rats and mice, to be composed of four rings of 16 sectors each. Central to the design of the insert are sensitivity above 15% and spatial resolution below 1 mm, both of which are necessary for target applications including dynamic brain and cardiac imaging. To achieve this performance, the proposed system will have an 8 cm axial field-of-view with 2 cm thick crystal blocks, using depth-of-interaction (DOI) encoding detectors to limit parallax error. While not strictly necessary for mouse brain studies, DOI detectors are vital to maintain spatial resolution when imaging larger objects such as the rat torso, or when undertaking high throughput studies where multiple animals are imaged simultaneously. Various approaches to DOI encoding have been successfully incorporated into preclinical PET systems, most commonly multi-layer scintillating crystal arrays (Yamamoto *et al* 2012,

Omidvari *et al* 2017, Stortz *et al* 2018, Vrigneaud *et al* 2018), but also monolithic detectors (Sánchez *et al* 2012) and dual ended readout (Yang *et al* 2016). A comprehensive analysis of DOI encoding methods is provided by Ito *et al* (2011). The proposed system will use a dual-ended DOI encoding detector, targeting 4 mm DOI resolution, 15% energy resolution, and the ability to resolve 1 mm crystal elements in the detector. Although there exist higher resolution detectors, these specifications represent a reasonable balance between spatial resolution, sensitivity, and complexity considering the performance of previously characterized dual-ended DOI encoding detectors (Yang *et al* 2011, Ren *et al* 2014).

Although relatively high sensitivity systems (e.g. 9% @ 256 to 766 keV, Bruker PET/MR 3T) are now commercially available, the proposed geometry will provide 16% sensitivity for a line source with an energy window of 250 to 650 keV (GATE simulation, results not shown) (Jan *et al* 2004). These performance improvements will make the proposed system more capable of serving the applications best suited to combined PET/MRI (Wehrl *et al* 2013, Ouyang *et al* 2014). This paper describes the design of the detector module for our proposed system, reconciling the trade-offs inherent to dual-ended SiPM based detectors. These trade-offs include: improving separation of edge crystals while minimizing system dead space, minimizing crystal element pitch without degrading crystal separation, and improving DOI resolution without degrading energy resolution. Based on these trade-offs, we have identified the optimal arrangement of SiPM elements within the detector block, as well as a crystal array and surface treatment suitable for dual-ended DOI measurement. These components together provide a simple prototype that will scale to meet the necessary system performance.

Methods

Overview

To determine the combination of components yielding the best performance for our application, we first tested cerium-doped lutetium-yttrium oxyorthosilicate (LYSO) arrays, fabricated by Crystal Photonics Inc. as well as lutetium fine silicate (LFS) arrays, fabricated by Zecotek Photonics. All LFS arrays were LFS-3. The first objective of our characterization was to identify the crystal material and pitch best suited for our applications, using a single surface treatment and SiPM array geometry.

To optimize DOI encoding, we then tested arrays fabricated with either Toray reflector or enhanced specular reflector (ESR) together with lapped or polished surfaces. In this evaluation, only LYSO arrays were tested, using a single SiPM array geometry.

Finally, various SiPM array geometries were tested in combination with the optimized crystal array. Each detector module included a front and rear SiPM array. The front side array had a transverse width smaller than the face of the crystal block to reduce system dead space, while the rear array had a slightly larger transverse width to improve crystal separation. Figure 1 shows the detector design and a module used for characterization. In each step of our characterization the detector was evaluated based on energy resolution, DOI resolution, and crystal separation.

Crystal array material and pitch—We have tested LYSO and LFS arrays as two candidate materials for the detector module. LFS is an appealing alternative to LYSO, having similar brightness and rise time and potentially lower cost (Grodzicka *et al* 2011). We have evaluated intrinsic performance of single LFS crystals, as well as positioning and DOI performance of LFS and LYSO arrays. Acquisitions were performed using arrays with three different element pitches: 0.87, 1.07, and 1.27 mm for LFS, and 0.80, 1.00, and 1.20 mm for LYSO. The LFS arrays had $22 \times 22, 18 \times 18$, and 15×15 elements, and a footprint of about 19×19 mm^2. The LYSO arrays had only 10×10 elements to reduce cost. All crystal arrays were 20 mm long. To properly investigate edge effects, the smaller LYSO arrays were positioned in corner of the SiPM arrays, near to where the edge of a full-sized 19×19 mm^2 array would sit in the completed detector. Both sets of crystal arrays had polished surfaces and used 70 µ*m* thick Toray reflector, which provides a reasonable compromise between energy and DOI resolution (Ren *et al* 2014).

Based on preliminary measurements, we selected rectangular 5×6 and 5×4 SiPM arrays to read out the LYSO and LFS arrays. The SiPM array geometry is shown in table 3. Although the SiPM array plays a significant role in absolute detector performance, we expect that the choice is independent of the relative performance of the crystal arrays, especially for energy and DOI resolution.

Crystal array surface treatment and reflector—We tested Toray reflector and ESR, in combination with lapped and polished surface finishes. Optical glue was used to couple the reflector to the crystal surface. Both reflectors had 70 µ*m* thickness, but material properties are proprietary manufacturer and are not readily available. Detailed specifications for the rough lapped and polished surface treatments are similarly unavailable. A general discussion of reflector properties is available from Janecek and Moses (2008), establishing the specular nature of ESR and the mixed behavior of Toray reflectors. The role of surface roughness in determining light output has been similarly characterized by Roncali and Cherry (2013). Three of the four possible combinations of surface treatment and reflector were characterized. The combination of polished surface and ESR reflector was not tested due to its known poor DOI performance (Ren *et al* 2014). All arrays used LYSO with 10×10 elements, 1.0 mm pitch, 20 mm length, and were read out using the 5×6 and 5×4 SiPM array configuration.

SiPM array geometry—After identifying the crystal array most suitable for our application, we characterized several SiPM array geometries to optimize energy resolution, DOI resolution, and separation of edge crystals. Custom geometry SiPM arrays were designed with 3×3 mm2 SensL J series SiPMs (MicroFJ-30035-TSV, SensL, Ireland) as previously described by Kyme *et al* (2017). The SiPM arrays varied in packing fraction and how far they extended past the edge of the crystal block, two key geometric factors governing performance of block detectors with light sharing. Increasing SiPM array packing fraction improves light collection, while increasing the extent of the SiPM array past the edge of the crystal block improves separation of edge crystals. Different geometries were realized by increasing gap sizes between SiPM elements, which also reduces detector cost but may create artifacts due to sparsity and asymmetric coverage of the crystal block faces.

By varying the number and pitch of SiPM elements in each photodetector array, we have characterized the role of sparsity in dual-ended DOI encoding detectors and selected an optimal combination for both front and rear arrays.

Square SiPM arrays have been used with positive outcomes in many existing systems. Separation of edge crystals, however, generally requires that the SiPM overhang the crystal array, introducing angular dead-space when detectors are arranged edge-to-edge in a ring. Compared to square arrays, rectangular arrays may improve edge crystal separation while minimizing this dead-space, contributing a 1.2 fold increase in system sensitivity in preliminary simulations. In the configuration illustrated in figure 1, the front and rear SiPM arrays have equal axial extent, but the front array does not overhang the crystal block transaxially The rear array, however, overhangs the crystal block transaxially by several millimeters, improving separation of edge crystals. This configuration minimizes spacing between the front edges of adjacent crystal arrays. Both square and rectangular arrays were tested with pitches chosen to leave either 1 or 2 crystals of axial dead space in the completed system, corresponding to either 0.5 or 1 mm overhang of the SiPM array. Table 3 summarizes the SiPM array configurations.

Having previously identified the optimal crystal array material, pitch, and surface treatment, we obtained a full-sized crystal array with a geometry matching that which we plan to use in the completed system. The array used LYSO crystals with polished surface and Toray reflector, and had 19×19 elements with 1.0 mm pitch and 20 mm length ($0.93 \times 0.93 \times 20$ mm^3 element size). This array was used to characterize each of the SiPM array configurations.

Detector characterization and experimental setup

Crystal and SiPM arrays were coupled with 1.0 mm acrylic light guides and optical grease. SiPM array signals were multiplexed with an Anger resistive network, yielding eight signals between the front and rear arrays (Siegel *et al* 1996). *X* and *Y* positions were calculated independently for the two arrays and the average of the two values was used to generate flood histograms. Other positioning methods may yield clearer flood histograms depending on SiPM array geometry, but this method provides an unbiased assessment for all configurations. Anger charge division schemes resolve as many crystals as alternative approaches, but cause pincushion distortion of the flood histogram (Shah *et al* 2002). Row-column charge division and similar approaches may improve crystal separation and reduce distortion at the cost of more readout channels, as previously demonstrated (Kyme *et al* 2017).

Each corner signal was fed through a preamplifier (Analog Devices, AD8055) and then split into fast and slow shaping amplifiers (Texas Instruments, OPA2694). The four fast signals were summed and passed through a NIM fan-in module (Phillips Scientific 740) and constant fraction discriminator (Phillips Scientific 715) to produce a timing signal. The timing signal was fed into a logic unit (Phillips Scientific 756) to generate a trigger signal for the DAQ and a reference for coincidence measurements. Slow signals were passed to a spectroscopic amplifier (CAEN, N68B) and subsequently to the DAQ cards (United Electronics Industries) which sampled the peak amplitude of coincident event waveforms

according to the timing signal (Judenhofer *et al* 2005). Coincidence acquisitions were performed using a 0.5 mm thick LYSO reference detector, providing electronic collimation. A sealed ^{22}Na point source with 0.25 mm active diameter and approximately 50 μCi (1.85 MBq) activity was used for each acquisition (Eckard & Ziegler Isotope Products). Acquisitions spanned 9 DOI positions at 2 mm increments collecting approximately 1000 events per crystal. No events were acquired at the outermost DOI positions due to uncertainty in alignment of the experimental and reference detectors. Subsequently, the 2 and 18 mm DOI positions are not included in plots of energy or DOI resolution. All acquisitions were performed at room temperature with 29.5 V SiPM bias for both arrays, about 5 V over breakdown.

The eight energy signals per event yielded energy and DOI spectra at each interaction depth. Energy and DOI resolution were analyzed per-crystal by segmenting the flood histogram to generate a crystal lookup table. When edge crystals were not distinctly resolved, they were not included when calculating the mean energy and DOI resolution for the array. To calculate energy resolution, the photopeak of each energy spectra was fitted with a Gaussian curve, yielding a FWHM and photopeak position. No correction for SiPM saturation was applied, since the light sharing geometry and DOI encoding crystal array both limit total light collection. The DOI ratio for each event was calculated as the energy of the rear detector divided by the sum of the front and rear energy. A linear regression between the DOI ratio peak and the known DOI position of an acquisition allows for calculation of the FWHM DOI resolution in millimeters (Ren *et al* 2014). A complimentary measure of DOI resolution, the DOI classification accuracy, was used to assess the magnitude of non-Gaussian features in the DOI spectra. The classification accuracy was calculated as the integral of the DOI spectra over a 4 mm window around the peak, divided by the integral of the DOI spectra over the full length of the crystal (figure 2). This approach yields the same information as the FWHM if the distribution is Gaussian, as 76% of events will fall within the FWHM. For distributions with non-Gaussian tails, however, the classification accuracy will decrease as magnitude of the tails increase. The 4 mm window was chosen as a conservative estimate of DOI spectra FWHM based on previously reported performance of similar detectors (Ren *et al* 2014).

For data presented in box and whisker plots, hinges indicate the boundaries of the first and third quartiles, while whiskers extend to the point nearest but not greater than 1.5 times the difference between the first and third quartiles. The center line indicates the median of all crystals in the array. Outlying crystals have been omitted from the plot for clarity but are included in the tables.

Results

Crystal array material and pitch

Preliminary characterization of single $3 \times 3 \times 20$ mm^3 LFS crystal coupled to an SiPM yielded an energy resolution of 9.47%. Table 1 summarizes the performance of both LFS and LYSO arrays at multiple crystal pitches. Of the LFS arrays, only the 1.27 mm pitch array was resolved to individual crystals, as shown in figure 3. Performance of the smaller 1.07 and 0.87 mm arrays was not quantified because they could not be segmented.

The LYSO arrays were well resolved, with some blurring of edge crystals for the smallest two arrays. Figure 4 provides a direct comparison of the energy and DOI performance at different irradiation depths for the largest LFS and LYSO arrays. Despite the improved DOI FWHM of LFS, the overall classification accuracy of the two materials did not suggest a significant difference in performance. Figure 5 shows peak position of the DOI ratio for the two materials, the dynamic range of which is larger for LFS.

Each of the three LYSO arrays showed good performance, with an energy resolution of 13.3% ± 1.89% for the largest crystals. The DOI resolution for the 1.2 mm pitch array was on average 3.05 ± 0.51 mm, degrading to 3.55 ± 0.77 mm for the 0.8 mm pitch array. The measured DOI classification accuracy followed a similar trend to the FWHM.

Crystal array surface treatment and reflector

Each of the three surface treatments had distinctly different performance, as summarized in table 2 and illustrated in figure 6. The lapped/ESR combination resulted in an average energy resolution of 11.5% but also showed FWHM DOI resolution worse than 10 mm. The surface finishes using Toray had an average energy resolution of 14.8% and 14.5% and DOI resolution of 2.37 and 3.36 mm for lapped and polished surfaces, respectively. Although none of the configurations resolved the rightmost edge crystals, the polished/Toray configuration yielded floods with the clearest overall separation (figure 7).

SiPM array pitch and geometry

Table 3 summarizes the SiPM array configurations which were tested. Figure 8 shows selected flood histograms for different SiPM array configurations as well as line profiles through a center row of crystals. The rectangular SiPM array (highlighted in table 3) was the only configuration to fully resolve the 19 × 19 crystal array. Edge crystals in the horizontal (axial) direction were resolved but showed relatively low peak-to-valley ratios, while crystals in the vertical (transaxial) direction were well resolved due to the greater extent of the rear 5 × 6 array. Figure 9 illustrates in detail the relationship between DOI resolution and energy resolution for three SiPM array geometries selected from table 3.

Discussion

Crystal array material and pitch

Single LSF crystals show 9.47% energy resolution and light output comparable to LYSO, making LFS a promising material for the proposed detector. These LFS arrays, however, have persistently worse energy resolution than LYSO (figure 4). Furthermore, even when using SiPM arrays with a large extent past the edge of the crystal block, crystal arrays with pitch smaller than 1.2 mm were poorly resolved (figure 3). This performance may relate to differences in the light output of LFS and LYSO arrays, resulting from optical properties of the reflector material or glue used during assembly. This possibility is supported by differences in the FWHM DOI resolution for the two materials (figure 4). Reflector materials and surface treatments with stronger diffusive properties generally reduce light output, degrading energy resolution and improving DOI encoding (Roncali and Cherry 2013). The degree of DOI encoding is further manifest in the dynamic range of the DOI

ratio spectra, which is wider for the LFS arrays (figure 5). Differences in light output further explain the nonuniform appearance of LFS crystals in figure 3, resulting from insufficient light sharing between SiPMs. With very little light output, only one SiPM produces a measurable signal following scintillation events, causing crystals to appear clustered around their nearest SiPM. Differences in flood histogram quality ultimately excluded LFS as an option for the proposed detector. LFS remains a promising material for future preclinical systems, but improvements in array fabrication are necessary to take advantage of its material properties.

Although energy and DOI resolution of the LYSO arrays improved with larger crystal pitch, indicated by figure 10, edge crystal separation was the strongest differentiator of performance among the crystal arrays. The 0.8 mm array had relatively poor separation of edge crystals, and is similar to what has been shown previously with other readout circuits (Kyme *et al* 2017). Although the 1.2 mm array was fully resolved, similar resolution of the 1.0 mm array may be achieved after optimization of the detector light guide and methods for calculating the flood histogram. This potential for further improvement favors the 1.0 mm pitch LYSO array for the final detector module.

Crystal array surface treatment and reflector

The performance of ESR coupled arrays agrees with previous studies, showing very little encoding of DOI information (Ren *et al* 2014). Figure 6 shows a strong trend in the depth-dependent DOI resolution when Toray is used with either a lapped or polished surface. The lapped surface yields its best DOI encoding at the ends of the array, contrasting the polished surface which performs best at the center. Patterns of reflection and absorption for each material may account for these trends, and have previously been assessed in simulation (Roncali and Cherry 2013). Ultimately, improved DOI resolution of the lapped finish comes at the cost of degraded crystal separation, visible in the line profile in figure 7. We expect that the 3.5 mm DOI resolution of the polished/Toray array is sufficient to maintain homogenous spatial resolution throughout the FOV of the proposed PET/MRI insert.

Energy resolution also shows a depth dependent trend, as in figures 4, 6, 9 and 10. This trend results from depth dependence of the single ended energy resolution, which is worst for DOI positions nearest the photodetector (Yang *et al* 2011). When measures from each end are summed, energy resolution is best at the center of the crystal. Depth dependence of the energy resolution can be reduced by calculating energy as the geometric mean of the front and rear values (Ren *et al* 2014). Energy resolution is less depth dependent for arrays coupled with ESR than those with Toray, possibly due to differences in light extraction (figure 6).

SiPM array geometry

Packing fraction of the various SiPM arrays conveys a small but noticeable effect on detector energy and DOI resolution, evident in figure 9. The $5 \times 5, 6 \times 6$ array configuration, which has the highest packing fraction of all tested configurations, shows the best energy and DOI resolution, with up to 4.0% and 0.92 mm improvement over the sparsest $4 \times 4, 5 \times 5$ configuration. Although the FWHM DOI resolution improves with increasing packing

fraction, the same patterns are not observed in classification accuracy. Given that the FWHM of a Gaussian distribution contains 76% of events, classification accuracy will increase as FWHM decreases for a fixed acceptance window. That the classification accuracy does not reach 70% for any of the arrays tested indicates that non-Gaussian tails or other features of the DOI spectra counteract the factors improving the FWHM DOI resolution. The same is true in the analysis of the crystal array geometry, surface treatment, and reflector, where classification accuracy trails what would be expected based on the FWHM.

Geometry of the SiPM arrays has the strongest effect on edge crystal separation. Without at least 0.5 mm of edge overhang, the outermost crystals are not resolved. Minimizing SiPM overhang, however, is necessary to limit the axial gap between detectors. Rectangular 5×6 and 5×4 SiPM arrays maximize transaxial crystal separation (vertical in figure 8), without increasing dead-space in the system. Axially (horizontal in figure 8), both front and rear arrays are dimensioned to allow for approximately 0.5 mm extent of SiPM array, resulting in a 1 mm axial gap between neighboring arrays. Square geometries achieving similar edge crystal separation would require an axial gap greater than 4 crystals, which is unfavorable based on the constrained geometry of the proposed system and the requirement for high sensitivity. Based on these considerations, the 5×6, 5×4 SiPM arrays are best suited to the requirements of the proposed system.

Considering recent publications characterizing the performance of SensL SiPMs in high magnetic fields, we have not performed characterization of this detector module within an MRI (Goertzen *et al* 2016). We do not expect significant performance changes when operating this detector inside a magnetic field or during MRI gradient operation. Additional factors which have not been addressed in this study are the optimization of light guides, SiPM multiplexing, and readout methods. Each of these aspects will have some impact on the detector energy resolution, DOI resolution, and crystal separation. Optimizing the light guide can further enhance crystal separation, with the light guide thickness adjusted based on the SiPM array pitch and surface cuts altering the light distribution of edge crystals. Selection of an optimal readout circuit will depend on the channel density of the readout electronics and necessary dead-time performance. The Anger readout used here has a high degree of channel reduction and good dead-time due to the small solid angle coverage of each detector. Row-column multiplexing circuits may produce better flood histograms, but require more readout channels and data corrections depending on the block size (Kyme *et al* 2017).

Conclusions

Our optimized detector uses rectangular SiPM arrays with 5×6 and 5×4 elements for the front and rear photodetectors, coupled to a 19×19 array of 1 mm pitch LYSO crystals with polished surfaces and Toray reflector. The prototype design has 14.3% ± 2.9% energy resolution, 3.57 ± 0.88 mm DOI resolution, and resolves all elements in the crystal array.

The detector described here differs from previously published designs in its prioritization of sensitivity through the use of a 2 cm thick crystal array. Custom SiPM arrays provide a reliable readout, facilitating clear separation of crystal elements and accurate event

positioning. The high degree of SiPM signal multiplexing, finally, minimizes the number of readout channels per block without compromising performance. Together these characteristics serve as the foundation for the design of the proposed PET/MRI insert.

Acknowledgments

References

Disselhorst JA, Bezrukov I, Kolb A, Parl C and Pichler BJ 2014 Principles of PET/MR imaging J. Nucl. Med 55 2S–10S [PubMed: 24819419]

Goertzen AL et al. 2016 First results from a high-resolution small animal SiPM PET insert for PET/MR imaging at 7T IEEE Trans. Nucl. Sci 63 2424–33

Grodzicka M et al. 2011 Characterization of LFS-3 scintillator in comparison with LSO Nucl. Instrum. Methods Phys. Res. A 652 226–30

Hallen P. et al. 2018; PET performance evaluation of the small-animal hyperion II^D PET/MRI insert based on the NEMA NU-4 standard. Biomed. Phys. Eng. Express. 4

Ito M, Hong SJ and Lee JS 2011 Positron emission tomography (PET) detectors with depth-of-interaction (DOI) capability Biomed. Eng. Lett 1 70

Jan S et al. 2004 GATE—Geant4 application for tomographic emission: a simulation toolkit for PET and SPECT Phys. Med. Biol 49 4543–61 [PubMed: 15552416]

Janecek M and Moses WW 2008 Optical reflectance measurements for commonly used reflectors IEEE Trans. Nucl. Sci 55 2432–7

Judenhofer MS, Pichler BJ and Cherry SR 2005 Evaluation of high performance data acquisition boards for simultaneous sampling of fast signals from PET detectors Phys. Med. Biol. 50 29 [PubMed: 15715420]

Ko GB et al. 2016a Evaluation of a silicon photomultiplier PET insert for simultaneous PET and MR imaging Med. Phys 43 72–83 [PubMed: 26745901]

Ko GB et al. 2016b Simultaneous multiparametric PET/MRI with silicon photomultiplier PET and ultra-high-field MRI for small-animal imaging J. Nucl. Med 57 1309–15 [PubMed: 27081173]

Kyme AZ. et al. 2017; Open-field mouse brain PET: design optimisation and detector characterisation. Phys. Med. Biol. 62:6207. [PubMed: 28475491]

Mackewn JE et al. 2015 PET performance evaluation of a pre-clinical SiPM-based MR-compatible PET scanner IEEE Trans. Nucl. Sci 62 784–90

Mannheim JG et al. 2018 PET/MRI hybrid systems Semin. Nucl. Med 48 332–47 [PubMed: 29852943]

Omidvari N. et al. 2017; PET performance evaluation of MADPET4: a small animal PET insert for a 7 T MRI scanner. Phys. Med. Biol. 62:8671. [PubMed: 28976912]

Ouyang Y. et al. 2015; Simultaneous PET/MRI imaging during mouse cerebral hypoxia-ischemia. J. Vis. Exp. JoVE. 103:e52728.

Ouyang Y, Tinianow JN, Cherry SR and Marik J 2014 Evaluation of 2-[18F]fluoroacetate kinetics in rodent models of cerebral hypoxia- ischemia J. Cereb. Blood Flow Metab 34 836–44 [PubMed: 24517980]

Ren S, Yang Y and Cherry SR 2014 Effects of reflector and crystal surface on the performance of a depth-encoding PET detector with dual-ended readout Med. Phys 41 072503 [PubMed: 24989406]

Roncali E and Cherry SR 2011 Application of silicon photomultipliers to positron emission tomography Ann. Biomed. Eng 39 1358–77 [PubMed: 21321792]

Roncali E and Cherry SR 2013 Simulation of light transport in scintillators based on 3D characterization of crystal surfaces Phys. Med. Biol 582185

Sánchez F et al. 2012 Small animal PET scanner based on monolithic LYSO crystals: performance evaluation Med. Phys 39 643–53 [PubMed: 22320773]

Shah KS, Farrell R, Grazioso R, Harmon ES and Karplus E 2002 Position-sensitive avalanche photodiodes for gamma-ray imaging IEEE Trans. Nucl. Sci 49 1687–92

Siegel S, Silverman RW, Shao Y and Cherry SR 1996 Simple charge division readouts for imaging scintillator arrays using a multi-channel PMT IEEE Trans. Nucl. Sci 43 1634–41

Stortz G et al. 2018 Performance of a PET insert for high-resolution small-animal PET/MRI at 7 Tesla J. Nucl. Med 59 536–42 [PubMed: 28912147]

Vrigneaud JM. et al. 2018; Initial performance evaluation of a preclinical PET scanner available as a clip-on assembly in a sequential PET/MRI system. Phys. Med. Biol. 63:125007. [PubMed: 29762132]

Wehrl HF et al. 2013 Simultaneous PET-MRI reveals brain function in activated and resting state on metabolic, hemodynamic and multiple temporal scales Nat. Med 19 1184–9 [PubMed: 23975025]

Weissler B et al. 2015 A digital preclinical PET/MRI insert and initial results IEEE Trans. Med. Imaging 34 2258–70 [PubMed: 25935031]

Yamamoto S et al. 2012 Development of a flexible optical fiber based high resolution integrated PET/MRI system Med. Phys 39 6660–71 [PubMed: 23127060]

Yang Y et al. 2011 Tapered LSO arrays for small animal PET Phys. Med. Biol 56 139–53 [PubMed: 21119228]

Yang Y et al. 2016 A prototype high-resolution small-animal PET scanner dedicated to mouse brain imaging J. Nucl. Med 57 1130–5 [PubMed: 27013696]

Yoon HS et al. 2012 Initial results of simultaneous PET/MRI experiments with an MRI-compatible silicon photomultiplier PET scanner J. Nucl. Med 53 608–14 [PubMed: 22414638]
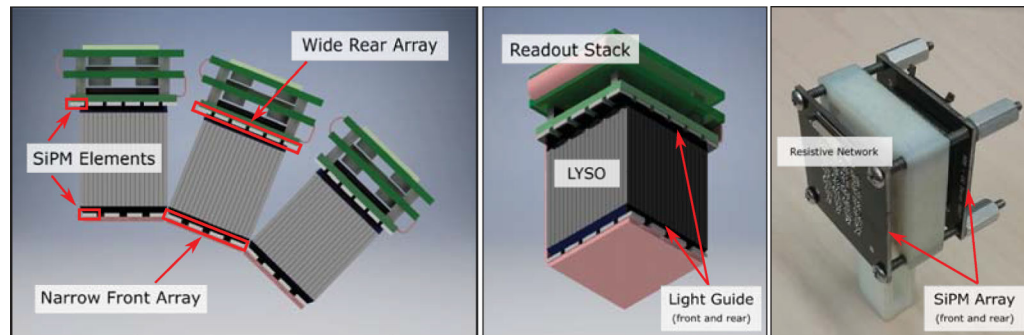
Figure 1.
Left: orientation of three blocks, illustrating the increased edge overhang of the rectangular SiPM array configuration. Center: 3D rendering of the proposed detector and readout stack. The rear SiPM array overhangs the LYSO block to improve edge crystal separation without a significant increase in system dead space. Right: prototype detector module used for component evaluation.
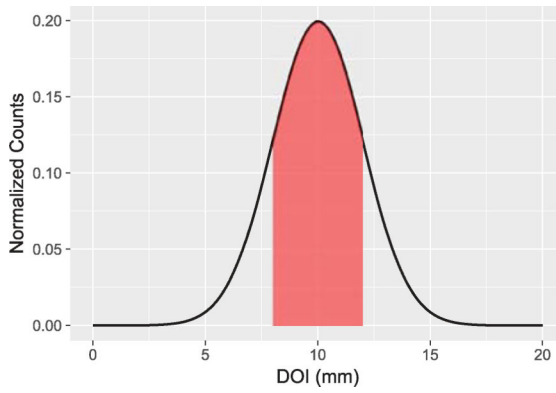
$$CA(DOI, x, w) = \frac{\int_{x-w/2}^{x+w/2} DOI(x')dx'}{\int_{0}^{L} DOI(x') \, dx'}$$

Figure 2.
Illustration of the method used to calculate classification accuracy. For a given DOI spectra, the classification accuracy (CA) is equal to the integral over a window (w, red shaded region) around the center DOI position (x), divided by the integral over the full length of the crystal (L).
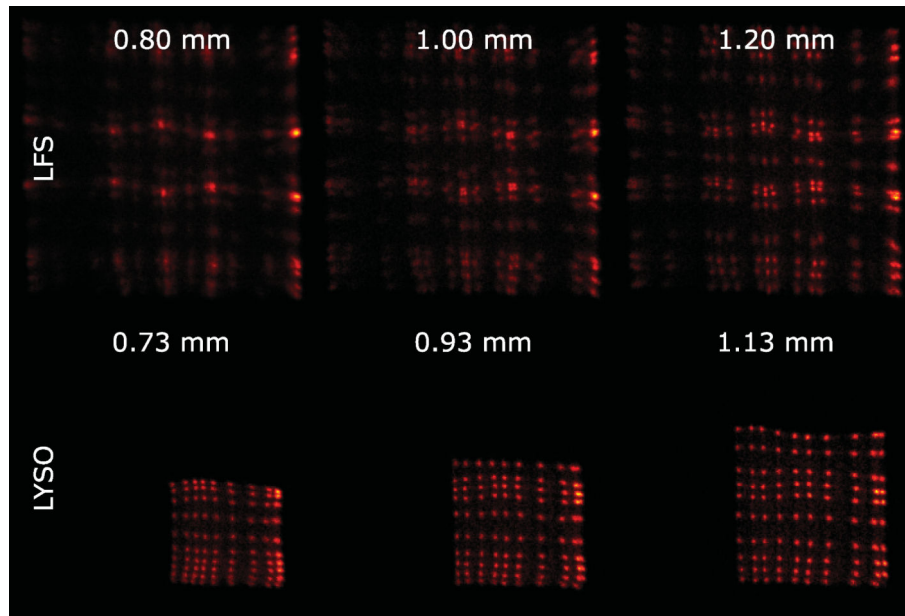
Figure 3.
Flood histograms for both LFS and LYSO at three crystal pitches. LYSO arrays had only ten elements, while LFS arrays were full sized.

Crystal array material
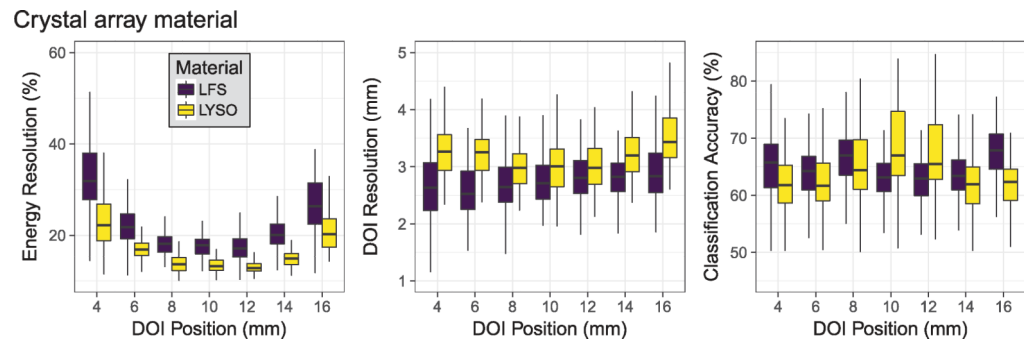
Figure 4.
Comparison of energy resolution, DOI resolution and DOI classification for LYSO and LFS materials. The LFS array had 1.27 mm pitch, while the LYSO array had 1.20 mm pitch. DOI classification accuracy assumes a 4 mm DOI range.
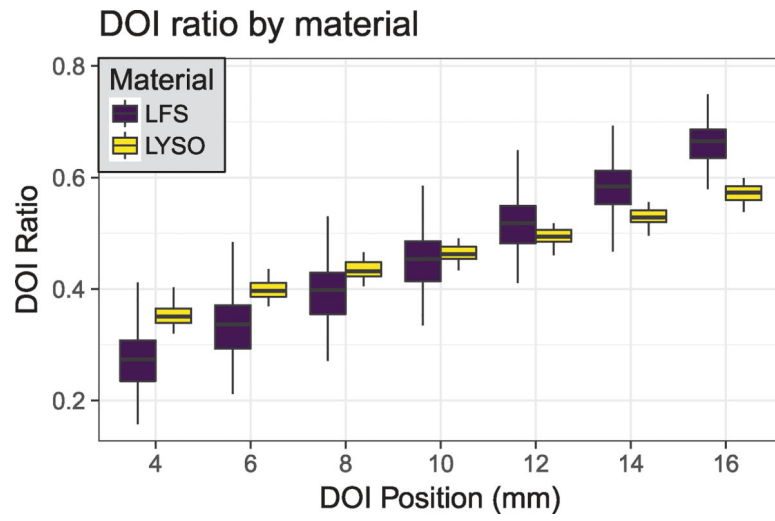
Figure 5.
DOI Ratio spectra peak for LFS and LYSO crystal arrays. Peak position was determined by fitting the spectra with a Gaussian function.

LYSO crystal array surface treatment
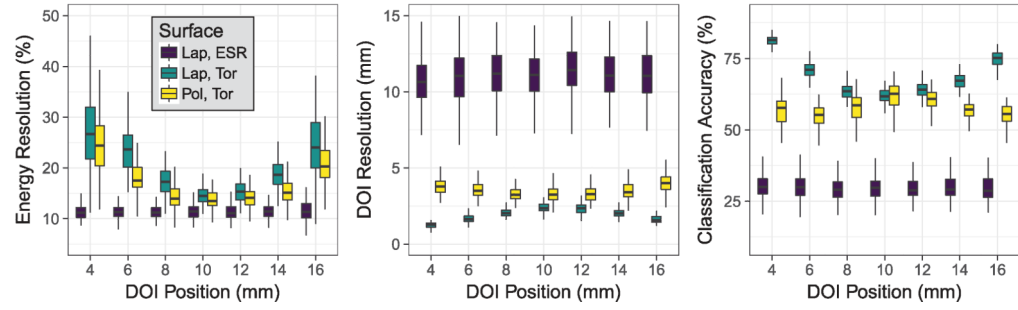
Figure 6.
Comparison of energy resolution, DOI resolution, and DOI classification performance for the three tested surface treatments.
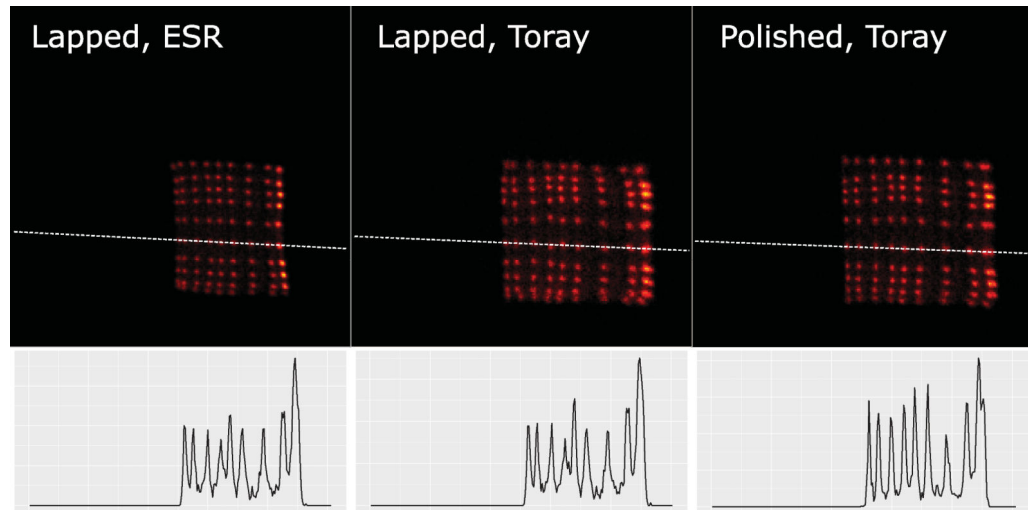
Figure 7.
Flood histograms for each of the surface treatments for the three LYSO arrays.
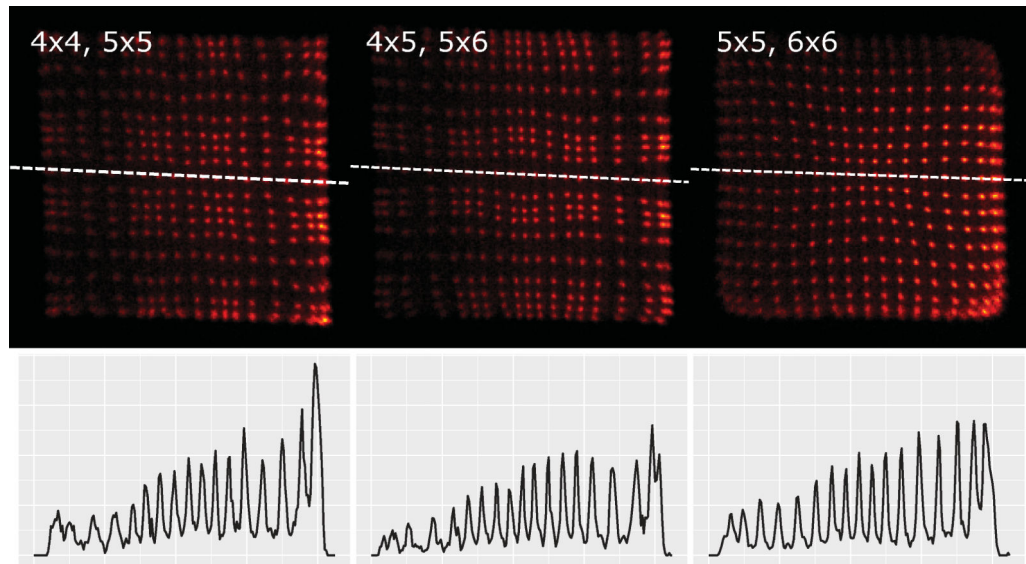
Figure 8.
Flood histograms and line profiles for three SiPM array configurations. Side-on irradiation results in nonuniform count rates across the array. Image scaling causes larger spot-size for the rightmost crystals and poorer contrast for the leftmost crystals.
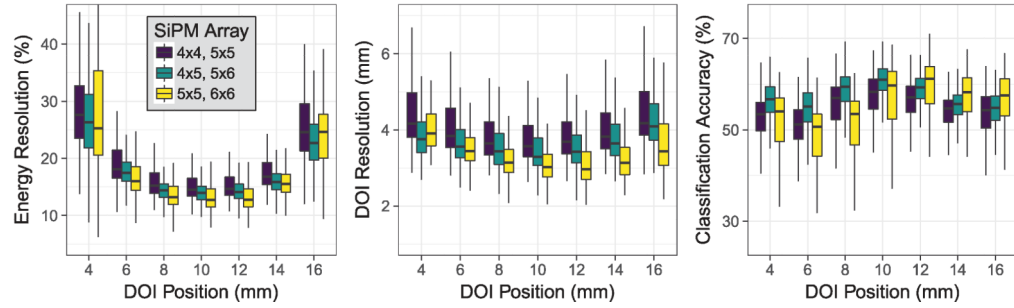
Figure 9.
Energy resolution, DOI resolution and DOI classification accuracy of three SiPM array configurations. The 4×4, 5×5 array configuration had an SiPM element pitch of 4.50 and 4.03 mm, respectively.

LYSO crystal array pitch
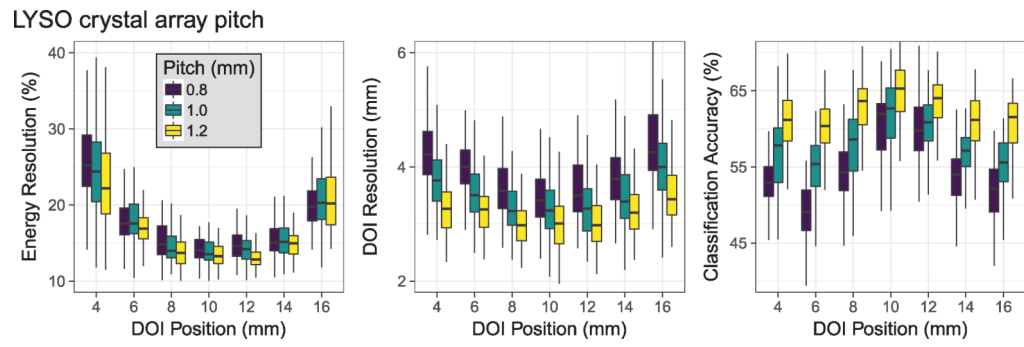
Figure 10.
Influence of LYSO crystal array pitch on energy resolution, DOI resolution and classification accuracy.

Table 1.

Summary of the performance of each crystal array at the 10 mm DOI position. All arrays had similar polished surfaces with Toray reflector and were read out with the 5×6 and 5×4 rectangular SiPM arrays.

Material	Elem. pitch (size), mm	Energy res. (%)	DOI res. (mm)	Resolved (total)
LFS	0.87 (0.80)	NA	NA	NA (22×22)
LFS	1.07 (1.00)	NA	NA	NA (18×18)
LFS	1.27 (1.20)	18.0 ± 3.4	2.74 ± 0.46	15×13 (15×15)
LYSO	0.80 (0.73)	15.4 ± 4.5	3.55 ± 0.77	10×9 (10×10)
LYSO	1.00 (0.93)	14.5 ± 5.4	3.36 ± 0.70	10×9 (10×10)
LYSO	1.20 (1.13)	13.3 ± 1.89	3.05 ± 0.51	10×10 (10×10)

Table 2.

Summary of performance for three LYSO crystal surface treatments at the 10 mm DOI position, read out with 5×6 and 5×4 rectangular SiPM arrays.

Surface finish	Reflector	Energy res. (%)	DOI res. (mm)	Resolved crystals
Lapped	ESR	11.5 ± 2.0	11.05 ± 1.90	10×9
Lapped	Toray	14.8 ± 2.1	2.37 ± 0.37	10×9
Polished	Toray	14.5 ± 5.4	3.36 ± 0.70	10×9

Table 3.

Summary of SiPM array performance. Each configuration was tested with the same 1.0 mm pitch 19×19 LYSO crystal array. Energy and DOI resolution are presented as the mean of all crystals at the 10 mm DOI position. Standard deviations are calculated based on the per-crystal variation across the array.

Front array	Front pitch (mm)	Rear array	Rear pitch (mm)	Energy res. (%)	DOI res. (mm)	Resolved crystals
4×4	4.50	5×5	4.03	15.2 ± 6.0	3.75 ± 1.16	17×17
4×4	4.90	5×5	4.03	15.4 ± 7.7	3.92 ± 1.01	17×17
4×4	4.50	5×5	4.48	16.5 ± 8.2	3.90 ± 1.26	17×17
4×4	4.90	5×5	4.48	17.8 ± 9.8	4.15 ± 1.53	17×17
4×4	4.50	6×6	3.60	13.9 ± 3.3	3.64 ± 1.18	17×17
4×4	4.90	6×6	3.60	14.1 ± 3.4	3.70 ± 1.01	17×17
5×5	3.15	6×6	3.60	13.8 ± 5.6	3.23 ± 1.01	17×17
5×4	4.16, 4.86	5×6	4.16, 4.00	14.3 ± 2.9	3.57 ± 0.88	19×19